Lin *et al.*
EURASIP Journal on Advances in Signal Processing (2023) 2023:22
https://doi.org/10.1186/s13634-023-00976-6

EURASIP Journal on Advances in Signal Processing

RESEARCH Open Access

Nonorthogonal waveform assisted DOA estimation for joint MIMO sensing and communication

Luning Lin[1], Hang Zheng[1], Chengwei Zhou[1,2*], Shibo He[3] and Zhiguo Shi[1,4]

*Correspondence: zhouchw@zju.edu.cn

[1] College of Information Science and Electronic Engineering, Zhejiang University, Hangzhou 310027, China
[2] Key Laboratory of Collaborative Sensing and Autonomous Unmanned Systems of Zhejiang Province, Hangzhou 310015, China
[3] College of Control Science and Engineering, Zhejiang University, Hangzhou 310027, China
[4] International Joint Innovation Center, Zhejiang University, Haining 314400, China

Abstract

Conventional direction-of-arrival (DOA) estimation methods for multiple-input multiple-output (MIMO) joint sensing and communication system normally pursue high estimation accuracy and resolution by imposing orthogonal waveforms. However, such operation results in a deterioration of communication performance. In this paper, we propose a nonorthogonal waveform assisted DOA estimation algorithm, where an augmented virtual array is derived by exploiting the nonorthogonal MIMO communication waveforms, while a high communication rate can still be maintained. To estimate the round-trip sensing channels of each subcarrier, we utilize the transmitted symbols as pilot symbols, and obtain all the channel coefficients with a minimum mean square error solver. A virtual channel matrix can be formulated with these channel coefficients, which can be regarded as the samples of an augmented virtual array. Based on that, the subspace processing can be conducted for DOA estimation with fully nonorthogonal waveforms. Furthermore, the rank deficiency property of the equivalent signal matrix of the virtual array is analyzed when the distance of targets are identical. To address the problem, a Toeplitz reconstruction method is proposed to restore the rank of the rank-deficient equivalent signal matrix for DOA estimation. Simulations show that the proposed nonorthogonal waveform assisted DOA estimation algorithm outperforms the conventional methods in terms of resolution and accuracy, while maintaining a satisfactory computational efficiency.

Keywords: DOA estimation, Joint sensing and communication, Nonorthogonal waveform, Virtual channel matrix

1 Introduction

With the rapid development of fifth-generation (5G) and beyond networks, the concept of joint sensing and communication has gained growing popularity due to its ability to improve spectrum efficiency while reducing hardware and energy costs [1–6]. In a joint sensing and communication system, the communication infrastructure can be multiplexed for locating noncooperative targets with a wide sensing coverage [7–9]. More importantly, since higher frequencies have been adopted in communication base stations [10], the finite concentrated propagation paths will be characterized by a channel in the angular domain [11]. As such, non-cooperative target localization can be achieved

by estimating direction-of-arrival (DOA) of echoes using the communication waveform [12–18]. Therefore, it is important to develop suitable DOA estimation methods for the joint multiple-input multiple-output (MIMO) sensing and communication system to enable an effective target localization function.

The mainstream DOA estimation methods for joint MIMO sensing and communication can be categorized into two types. For the first type, the communication performance is the primary consideration. Thus, the transmitted waveforms between different transmit antennas are nonorthogonal to obtain a high communication rate, and the inter-element spacings of the transmit and receive arrays are both set to half signal wavelength following the MIMO communication framework [19]. In [20], DOA estimation of non-cooperative targets is achieved by incorporating an additional sensing beam, which consists a duplication of the current communication symbols to avoid interfering the communication process. Moreover, the DOA estimation performance within the multi-beam framework with different power allocation fraction is analyzed in [21, 22]. Different from the above methods which employ the echo of downlink signals from the base station, the uplink signals from a specific mobile user with known location are utilized for DOA estimation without the requirement of full-duplex capability for the transceiver [23]. More recently, a DOA estimation method for a 5G New Radio (NR) system for bistatic sensing is proposed in [24], where the transmit and the receive arrays are separately located at different base stations or user equipments. Although the first type of methods minimize the impact of additional sensing function on the communication performance, the DOA estimation performance for a MIMO system traditionally depends on the derivation of an augmented virtual array. However, the nonorthogonality of communication waveforms used in these methods prevents the virtual array derivation since the signals transmitted by different antennas cannot be separated at the receiver side, thereby limiting the DOA estimation performance.

On the other hand, the second type of DOA estimation methods focus on enhancing the accuracy and resolution of DOA estimation. In particular, in order to derive virtual arrays, orthogonal waveforms are adopted between different transmit antennas, and the inter-element spacing is configured the same as MIMO radar [25]. Meanwhile, the communication symbols are embedded in these orthogonal waveforms. An interleaving frame structure is designed to divide the subcarriers into several orthogonal groups [26, 27]. As such, a virtual array can be derived from the received symbols for DOA estimation. Furthermore, the beam scanning strategy is combined with the transmit power compensation for DOA estimation [28]. Moreover, the sparse antenna array configuration is exploited to achieve finer angular resolution for target localization [29]. To ensure the quality-of-service for multiple mobile users, the virtual array is derived from the orthogonal waveforms transmitted to different users instead of different antennas in a hybrid beamforming architecture [30]. However, all these methods require orthogonal transmitting to derive the virtual array at the cost of reducing the communication rate to certain extent. Therefore, it is still challenging to develop an effective DOA estimation method with a minimum communication performance loss in the joint MIMO sensing and communication system.

To solve this problem, a sparse signal recovery (SSR)-based DOA estimation method is proposed with a partially orthogonal signal processing model [31]. To be specific, most subcarriers are shared by all the transmit antennas to exploit the full spectrum

effectively, while each antenna possesses an exclusive subscarrier to derive the virtual array. While DOA estimation methods exploiting fully nonorthogonal waveforms are investigated in [32, 33], they deal with the imperfect orthogonality through prewhitening operation, rather than utilizing the nonorthogonality of MIMO communication waveforms to ensure the communication rate. Hence, DOA estimation with fully nonorthogonal communication waveforms is an open and urgent task.

In this paper, we propose a nonorthogonal waveform assisted DOA estimation algorithm for joint MIMO sensing and communication system, where a virtual array is derived from the fully nonorthogonal waveforms for DOA estimation with a high communication rate. The transmitted symbols are employed as pilot symbols to sense the non-cooperative targets, based on which the round-trip sensing channels of all the subcarriers are estimated separately. In order to derive an augmented virtual array, the estimated channels are reconstructed according to the geometry relationship between each pair of transmit and receive antenna. Then, the round-trip sensing channel coefficients of all the subcarriers are modeled into a virtual channel matrix, which can be regarded as the equivalent signals received by the virtual array. Furthermore, to solve the problem of rank deficiency of the equivalent signal matrix brought by the targets located at identical distance, we propose a Toeplitz reconstruction approach to compensate the rank of the equivalent signal matrix. Finally, the DOAs can be effectively estimated by the subspace processing for the virtual channel matrix. The proposed algorithm is compared to the conventional DOA estimation methods for joint MIMO sensing and communication system, which verify its superior estimation performance.

The rest of this paper is organized as follows. In Sect. 2, the architecture of the joint MIMO sensing and communication is introduced. Then, the DOA estimation algorithm with nonorthogonal waveform is proposed, and the computational complexity is analyzed in Sect. 3. We demonstrate simulation results in Sect. 4, and draw our conclusion in Sect. 5.

Notations: We use a, $\boldsymbol{a}$ and $\boldsymbol{A}$ to denote scalar, vector and matrix, respectively. The (i, j)-th element in the matrix $\boldsymbol{A}$ is denoted by $\boldsymbol{A}(i,j)$, the i-th row in $\boldsymbol{A}$ is denoted by $\boldsymbol{A}(i,:)$, and the j-th column in $\boldsymbol{A}$ is denoted by $\boldsymbol{A}(:,j)$. The rank of matrix $\boldsymbol{A}$ is denoted by $\mathrm{rank}(\boldsymbol{A})$. The operators $[\cdot]^{\mathrm{T}}$, $[\cdot]^{\mathrm{H}}$ and $[\cdot]^{*}$ represent transpose, Hermitian transpose and conjugation, respectively. We denote a diagonal matrix as $\mathrm{diag}(\cdot)$. The Frobenius norm is denoted by $\|\cdot\|_{\mathrm{F}}$, the minimum is denoted by $\min(\cdot)$, the statistical expectation is denoted by $\mathrm{E}\{\cdot\}$, and the rounding down operator is denoted by $\lfloor\cdot\rfloor$. $\otimes$ and $\odot$ respectively denote the Kronecker and Hadamard products. Moreover, $\mathbf{0}$, $\mathbf{1}$ and $\boldsymbol{I}$ are the zero matrix, all-ones matrix and the identity matrix, respectively.

2 Joint MIMO sensing and communication system

As shown in Fig. 1, we consider a joint MIMO sensing and communication system equipped with N_t transmit antennas and N_r receive antennas, operating within the 5G Frequency Range 2 (FR2). Following the deployment of MIMO antenna array, the inter-element spacing of the receive array is $d_r = \lambda/2$ with λ being the signal wavelength, while the inter-element spacing of the transmit array is $d_t = N_r d_r$. The transmitted waveforms are utilized to communicate with mobile users and illuminate the non-cooperative targets, while the echoes reflected by these far-field targets are processed to estimate their DOAs.

An orthogonal frequency-division multiplexing (OFDM) frame with M OFDM symbols on K subcarriers is considered, where the total duration of each symbol regarding the cyclic

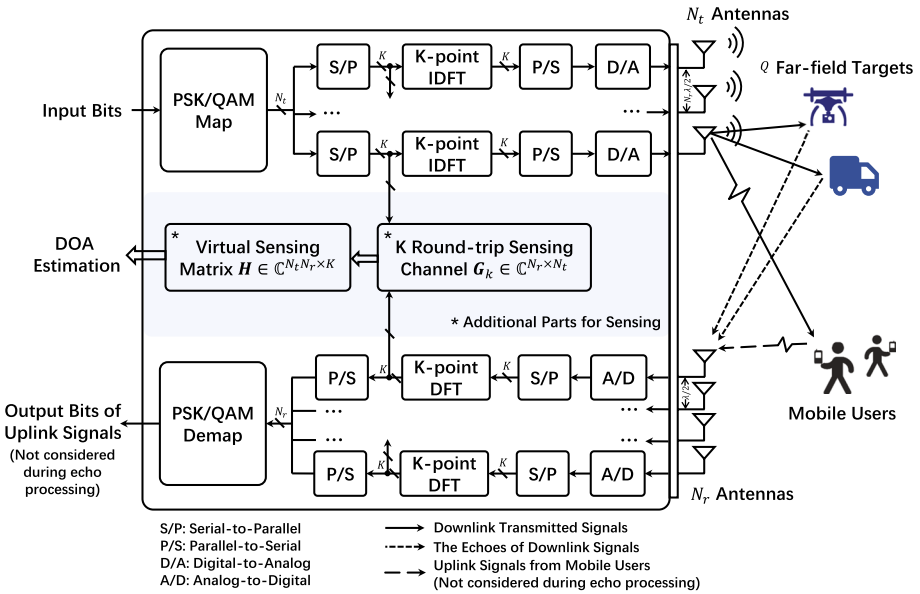

Fig. 1 Illustration of the deployed joint MIMO sensing and communication system

prefix (CP) is denoted by $T_{\text{sym}} = T + T_{\text{CP}}$. Here, T is the elementary symbol duration, and T_{CP} is the duration of CP. The m-th OFDM symbol transmitted by the array can be represented as

$$\begin{aligned} \boldsymbol{x}[m] &= \left[x_0[m], x_1[m], \cdots, x_{N_t-1}[m]\right]^{\text{T}} \\ &= \sum_{k=1}^{K} \boldsymbol{s}[k,m] e^{j2\pi k \Delta f m T_{\text{sym}}}, \end{aligned} \tag{1}$$

where $\Delta f = 1/T$ is the subcarrier spacing, and $\boldsymbol{s}[k,m] = [s_0[k,m], s_1[k,m], \cdots, s_{N_t-1}[k,m]]^{\text{T}}$ represents the complex data symbol vector modulated by phase-shift keying (PSK) or quadrature amplitude modulation (QAM), with $m = 0, 1, \cdots, M-1$ and $k = 1, 2, \cdots, K$ representing the indices of the OFDM symbol and subcarrier, respectively.

Assume that there are Q non-cooperative far-field targets with directions $\boldsymbol{\theta} = [\theta_1, \theta_2, \cdots, \theta_Q]^{\text{T}}$. The echoes reflected by these targets are sampled at the $(mT_{\text{sym}} + T_{\text{CP}} + k\frac{T}{K})$-th time slot for the m-th OFDM symbol. Then, the CP symbols are removed, and a K-point discrete Fourier transform (DFT) is applied to the obtained sample set of the m-th OFDM symbol. As such, the discrete representation of the received symbols in the frequency domain can be defined as

$$\boldsymbol{d}[k,m] = \underbrace{\boldsymbol{A}_r \boldsymbol{B} \text{diag}(\boldsymbol{e}_k) \boldsymbol{A}_t^{\text{T}}}_{\boldsymbol{G}_k} \boldsymbol{s}[k,m] + \boldsymbol{n}[k,m], \tag{2}$$

where $\boldsymbol{n}[k,m] \sim \mathcal{CN}\left(\boldsymbol{0}, \sigma_n^2 \boldsymbol{I}\right)$ is the additive white Gaussian noise vector, and

$$\boldsymbol{G}_k = \boldsymbol{A}_r \boldsymbol{B} \text{diag}(\boldsymbol{e}_k) \boldsymbol{A}_t^{\text{T}} \tag{3}$$

is the round-trip sensing channel of the k-th subcarrier. Here, $\boldsymbol{B} = \text{diag}(\beta_1, \beta_2, \cdots, \beta_Q)$ denotes a transmission attenuation matrix,

$$\boldsymbol{e}_k = [e^{-j2\pi k\Delta f\frac{2R_1}{c}}, e^{-j2\pi k\Delta f\frac{2R_2}{c}}, \cdots, e^{-j2\pi k\Delta f\frac{2R_Q}{c}}]^{\mathrm{T}} \tag{4}$$

is the round-trip delay of the k-th subcarrier, R_q is the distance between the q-th target and the deployed system, and $\boldsymbol{A}_t(\boldsymbol{\theta}) = \left[\boldsymbol{a}_t(\theta_1), \boldsymbol{a}_t(\theta_2), \cdots, \boldsymbol{a}_t\left(\theta_Q\right)\right]$, $\boldsymbol{A}_r(\boldsymbol{\theta}) = \left[\boldsymbol{a}_r(\theta_1), \boldsymbol{a}_r(\theta_2), \cdots, \boldsymbol{a}_r\left(\theta_Q\right)\right]$ are the transmit and receive steering matrices, where

$$\begin{aligned}\boldsymbol{a}_t\left(\theta_q\right) &= \left[1, e^{-j\frac{2\pi}{\lambda}d_t\sin\theta q}, \cdots, e^{-j\frac{2\pi}{\lambda}(N_t-1)d_t\sin\theta q}\right]^{\mathrm{T}},\\ \boldsymbol{a}_r\left(\theta_q\right) &= \left[1, e^{-j\frac{2\pi}{\lambda}d_r\sin\theta q}, \cdots, e^{-j\frac{2\pi}{\lambda}(N_r-1)d_r\sin\theta q}\right]^{\mathrm{T}}\end{aligned} \tag{5}$$

are the steering vectors corresponding to the q-th target, $q = 1, 2, \cdots, Q$. In the millimeter wave scenario considered in this paper, the subcarrier bandwidth is much smaller than the carrier frequency, i.e., $\Delta f \ll f_c$, which means that the difference between different subcarrier wavelength can be neglected, i.e., $\lambda = \frac{c}{f_c} \approx \frac{c}{f_c + k\Delta f}$. Here, f_c and c denotes the carrier frequency and the speed of light, respectively. Meanwhile, the uplink signals are not considered in (2), since the echoes of the downlink signals are expected to arrive before the end of the guard period (GP) under time division duplex (TDD) mode in FR2 band.

To exploit the available bandwidth, the deployed MIMO system transmits fully non-orthogonal waveforms as shown in Fig. 2c. Since all the K subcarriers are utilized by each transmit antenna, a maximum bit rate can be achieved as

$$R = (\log_2 4)KN_t/T_{\mathrm{sym}}. \tag{6}$$

In comparison, for the orthogonal and partially orthogonal transmitting principle demonstrated in Fig. 2a and Fig. 2b, the bit rates are $(\log_2 4)K/T_{\mathrm{sym}}$ and $(\log_2 4)(K-1)N_t/T_{\mathrm{sym}}$, which are both smaller than R in (6). Therefore, the fully non-orthogonal transmitting principle provides the highest communication rate. However, such a transmitting principle poses challenges on the derivation of augmented virtual array, which is essential to the MIMO system for enhancing source estimation performance [34–36]. To be specific, for the conventional methods with an orthogonal transmitting principle as shown in Fig. 2a, the m-th transmitted OFDM symbol can be represented as

$$\tilde{\boldsymbol{x}}[m] = \left[[\boldsymbol{s}[1,m], \boldsymbol{s}[2,m], \cdots, \boldsymbol{s}[K,m]] \odot \tilde{\boldsymbol{P}}\right] \begin{bmatrix} e^{j2\pi\Delta fmT_{\mathrm{sym}}} \\ e^{j2\pi 2\Delta fmT_{\mathrm{sym}}} \\ \vdots \\ e^{j2\pi K\Delta fmT_{\mathrm{sym}}} \end{bmatrix}, \tag{7}$$

where $\tilde{\boldsymbol{P}} = [\boldsymbol{I}_{N_t}, \boldsymbol{I}_{N_t}, \cdots, \boldsymbol{I}_{N_t}] \in \mathbb{C}^{N_t \times K}$ represents a subcarrier selection matrix, obeying a block-wise interleaving frame structure. In particular, $\tilde{\boldsymbol{P}}(:,k)$ has only one non-zero element, indicating the index of the transmit antenna of the k-th subcarrier. Hence, symbols transmitted on the k-th subcarrier all come from a certain transmit antenna. Moreover, $\tilde{\boldsymbol{P}}(n_t,:)$ has $\frac{K}{N_t}$ non-zero elements, indicating the subcarrier index $k \in \left\{n_t + zN_t + 1 \mid z = 0, 1, \cdots, \frac{K}{N_t} - 1\right\}$ possessed by the n_t-th antenna of the trans-

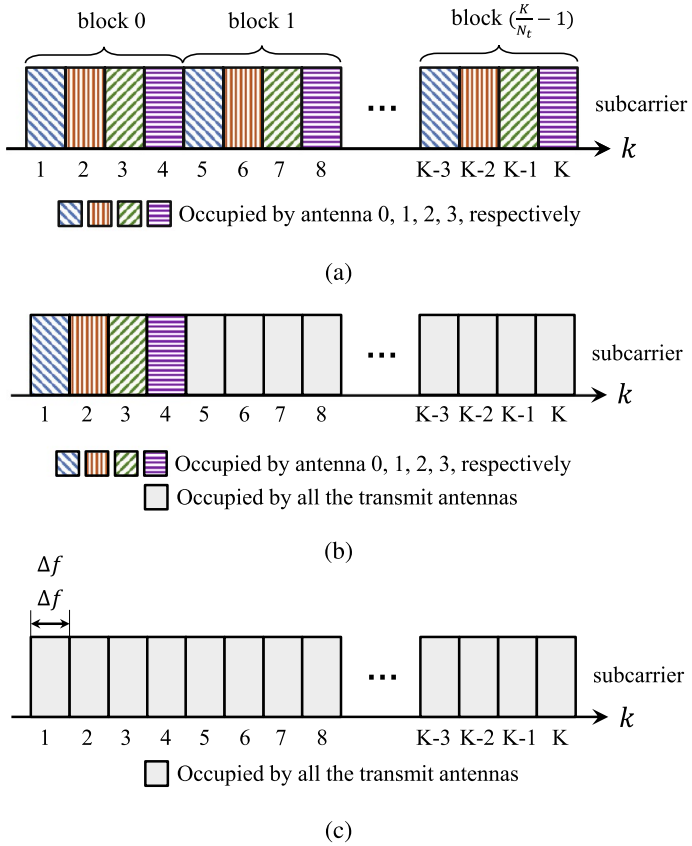

Fig. 2 Illustration of different transmitting principles. **a** Orthogonal transmitting; **b** Partially orthogonal transmitting; **c** Fully nonorthogonal transmitting

mit array. Here, z denotes the block index of the subcarriers as shown in Fig. 2a. Since different subcarriers can be separated by a set of matched filters at the receive array, $d_{n_r}[n_t + zN_t + 1, m]$ can be obtained for $s_{n_t}[n_t + zN_t + 1, m]$ at the n_r-th receive array antenna. After that, the sensing channel between the n_t-th transmit antenna and the n_r-th receive antenna is computed by an element-wise division as $i_{n_t,n_r}[z, m] = \frac{d_{n_r}[n_t+zN_t+1,m]}{s_{n_t}[n_t+zN_t+1,m]}$. Consequently, the sensing channel

$$\begin{aligned}\boldsymbol{i}[z,m] &= \left[i_{0,0}[z,m], i_{0,1}[z,m], \cdots, i_{n_t,n_r}[z,m], \cdots, i_{N_t-1,N_r-1}[z,m]\right] \\ &\approx \sum_{q=1}^{Q} \beta_q \left(\begin{bmatrix} e^{-j2\pi(0+zN_t+1)\Delta f \frac{2R_q}{c}} \\ e^{-j2\pi(1+zN_t+1)\Delta f \frac{2R_q}{c}} \\ \vdots \\ e^{-j2\pi(N_t-1+zN_t+1)\Delta f \frac{2R_q}{c}} \end{bmatrix} \odot \boldsymbol{a}_t \right) \otimes \boldsymbol{a}_r \end{aligned} \tag{8}$$

can be derived, which corresponds to a virtual array of size N_tN_r. Note that the virtual array derived from (8) is deviated from a uniform linear array (ULA), which is caused by various propagation delays on different subcarriers. Meanwhile, for the partially orthogonal transmitting principle as shown in Fig. 2b, the m-th transmitted OFDM symbol can be represented by $\tilde{\boldsymbol{x}}[m]$ in (7) by substituting $\tilde{\boldsymbol{P}}$ in (7) with $\acute{\boldsymbol{P}} = [\boldsymbol{I}_{N_t}, \boldsymbol{1}_{N_t\times(K-N_t)}]$. Here,

each column in $\acute{\boldsymbol{P}}(:, 1 : N_t)$ has only one non-zero element, which means that each transmit antenna possesses an exclusive subcarrier. As such, the virtual array derivation is also available in the partially orthogonal scenario.

However, in the considered fully nonorthogonal signal model as defined in (1) and (2), there are no exclusive subcarriers for each transmit antenna. As a result, the symbols transmitted by different antennas are mixed together in $\boldsymbol{d}[k, m]$, such that the construction of virtual array in (8) is no longer valid.

3 Proposed DOA estimation algorithm

In this section, we derive an augmented virtual array in the fully nonorthogonal scenario as shown in Fig. 3, based on which a nonorthogonal waveform assisted DOA estimation algorithm is proposed for the deployed joint MIMO sensing and communication system. Furthermore, we analyze the rank-deficiency problem of the equivalent signal matrix when targets are located at the same distance, and propose a suitable Toeplitz reconstruction solution.

3.1 Virtual channel matrix derivation for DOA estimation

The sensing channel, which depicts the attenuation and phase shift of the transmitted symbols during the round-trip propagation, contains all the information for virtual array derivation. Thus, to derive the virtual array, we estimate the round-trip sensing channel $\boldsymbol{G}_k$ in the nonorthogonal scenario through a minimum mean square error (MMSE) solver. First, we represent (2) in a compact form as

$$\boldsymbol{D}_k = \boldsymbol{G}_k \boldsymbol{S}_k + \boldsymbol{N}_k, \tag{9}$$

where $\boldsymbol{D}_k = [\boldsymbol{d}[k, 0], \boldsymbol{d}[k, 1], \cdots, \boldsymbol{d}[k, M-1]]$ is the OFDM demodulated symbol matrix, $\boldsymbol{S}_k = [\boldsymbol{s}[k, 0], \boldsymbol{s}[k, 1], \cdots, \boldsymbol{s}[k, M-1]]$ is the transmitted complex symbol matrix, $\Delta\boldsymbol{G}_k$ is the channel estimation error of the k-th subcarrier, and $\boldsymbol{N}_k$ is the noise matrix which satisfies $\mathrm{E}\{\boldsymbol{N}_k \boldsymbol{N}_k^{\mathrm{H}}\} = \sigma_n^2 M \boldsymbol{I}$. Then, the MMSE estimation for the sensing channel of the k-th subcarrier can be expressed as

$$\hat{\boldsymbol{G}}_k = \boldsymbol{D}_k \boldsymbol{W}_0, \tag{10}$$

where $\boldsymbol{W}_0$ minimizes the mean square error (MSE) of the estimation of sensing channel as

$$\boldsymbol{W}_0 = \arg\min_{\boldsymbol{W}} \mathrm{E}\left\{ \|\boldsymbol{G}_k - \boldsymbol{D}_k \boldsymbol{W}\|_{\mathrm{F}}^2 \right\}. \tag{11}$$

For the estimator $\boldsymbol{W}$, the sensing channel estimation error $\Delta\boldsymbol{G}_k$ can be represented as

$$\begin{aligned} \Delta\boldsymbol{G}_k &= \mathrm{E}\left\{ \|\boldsymbol{G}_k - \boldsymbol{D}_k \boldsymbol{W}\|_{\mathrm{F}}^2 \right\} \\ &= \mathrm{tr}\{\boldsymbol{R}_{\boldsymbol{G}_k}\} - \mathrm{tr}\{\boldsymbol{R}_{\boldsymbol{G}_k} \boldsymbol{S}_k \boldsymbol{W}\} - \mathrm{tr}\left\{ \boldsymbol{W}^{\mathrm{H}} \boldsymbol{S}_k^{\mathrm{H}} \boldsymbol{R}_{\boldsymbol{G}_k} \right\} \\ &\quad + \mathrm{tr}\left\{ \boldsymbol{W}^{\mathrm{H}} \left(\boldsymbol{S}_k^{\mathrm{H}} \boldsymbol{R}_{\boldsymbol{G}_k} \boldsymbol{S}_k + \sigma_n^2 M \boldsymbol{I} \right) \boldsymbol{W} \right\}, \end{aligned} \tag{12}$$

where $\boldsymbol{R}_{\boldsymbol{G}_k} = \mathrm{E}\{\boldsymbol{G}_k \boldsymbol{G}_k^{\mathrm{H}}\}$ is the matrix of sensing channel correlations. Then, the optimal $\boldsymbol{W}$, i.e., $\boldsymbol{W}_0$, can be obtained from $\partial(\Delta\boldsymbol{G}_k)/\partial\boldsymbol{W} = 0$ as

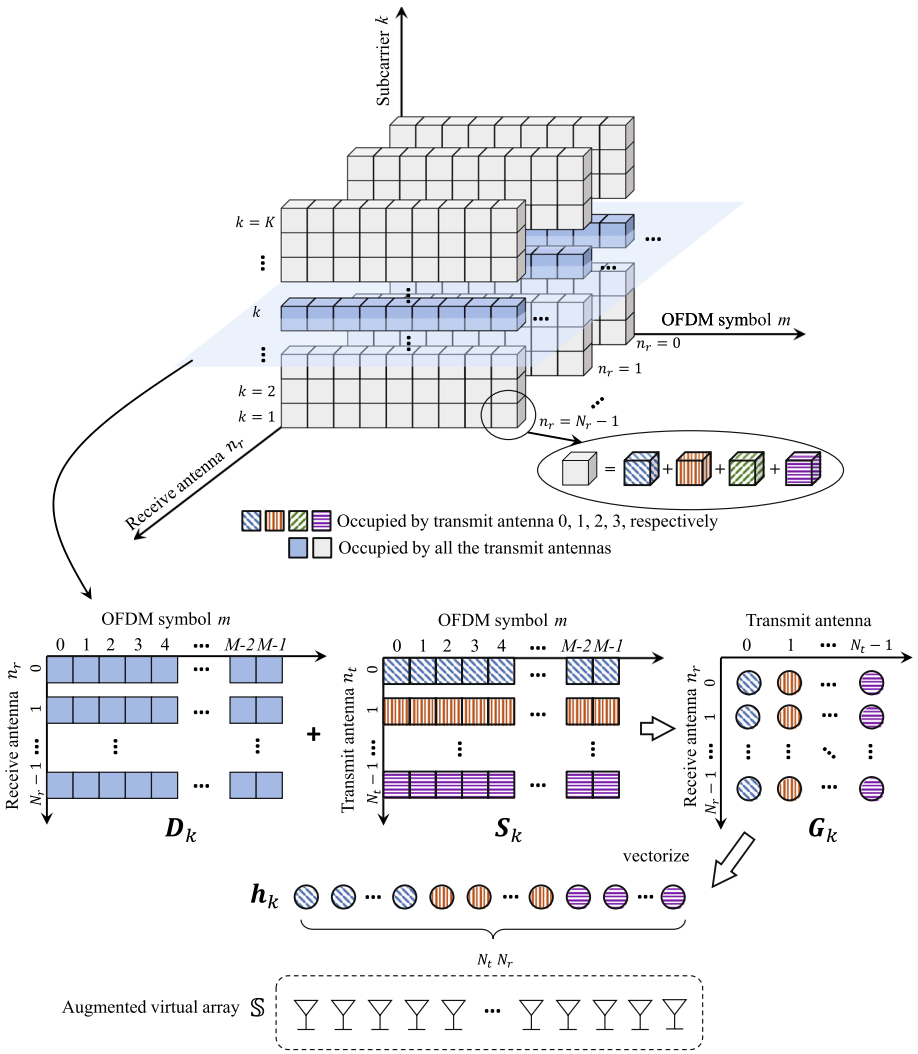

Fig. 3 Processing of the channel estimation in the fully nonorthogonal scenario

$$\boldsymbol{W}_0 = \boldsymbol{S}_k^{\mathrm{H}} \left(\boldsymbol{S}_k \boldsymbol{S}_k^{\mathrm{H}} + \sigma_n^2 M \boldsymbol{R}_{\boldsymbol{G}_k}^{-1} \right)^{-1}. \tag{13}$$

Hence, the estimated sensing channel on the k-th subcarrier can be obtained by substituting (13) into (10) as

$$\hat{\boldsymbol{G}}_k = \boldsymbol{D}_k \boldsymbol{S}_k^{\mathrm{H}} \left(\boldsymbol{S}_k \boldsymbol{S}_k^{\mathrm{H}} + \sigma_n^2 M \boldsymbol{R}_{\boldsymbol{G}_k}^{-1} \right)^{-1} = \boldsymbol{G}_k + \Delta \boldsymbol{G}_k. \tag{14}$$

Note that, we choose to estimate the round-trip sensing channel with MMSE estimator due to its conceptual simplicity and the effectiveness in utilizing the prior information. Nevertheless, there are some other channel estimation techniques that can be adopted, such as the linear minimum mean square error (LMMSE) method [37] with $\hat{\boldsymbol{G}}_k^{\mathrm{LMMSE}} = \boldsymbol{D}_k \boldsymbol{S}_k^{\mathrm{H}} \left(\mathrm{E}\{\boldsymbol{S}_k \boldsymbol{S}_k^{\mathrm{H}}\} + \sigma_n^2 M \boldsymbol{R}_{\boldsymbol{G}_k}^{-1} \right)^{-1}$, and least square (LS) method [38] with $\hat{\boldsymbol{G}}_k^{\mathrm{LS}} = \boldsymbol{D}_k \boldsymbol{S}_k^{\mathrm{H}} \left(\boldsymbol{S}_k \boldsymbol{S}_k^{\mathrm{H}} \right)^{-1}$.

It can be observed from (3) that, the round-trip sensing channel $\boldsymbol{G}_k$ is related to the transmit steering matrix $\boldsymbol{A}_t$ and the receive steering matrix $\boldsymbol{A}_r$. Due to the inter-element spacing settings inherited from the MIMO radar deployment, the Kronecker product of $\boldsymbol{A}_t$ and $\boldsymbol{A}_r$ would yield an equivalent virtual array. In this light, the estimated round-trip sensing channel $\hat{\boldsymbol{G}}_k$ can be vectorized as

$$\begin{aligned}\boldsymbol{h}_k &= \mathrm{vec}(\hat{\boldsymbol{G}}_k)\\ &= \mathrm{vec}(\boldsymbol{A}_r\boldsymbol{B}\mathrm{diag}(\boldsymbol{e}_k)\boldsymbol{A}_t^{\mathrm{T}}) + \mathrm{vec}(\Delta\boldsymbol{G}_k)\\ &= \boldsymbol{A}_{\mathbb{S}}(\theta_1,\theta_2,\cdots,\theta_Q)\boldsymbol{B}\boldsymbol{e}_k + \mathrm{vec}(\Delta\boldsymbol{G}_k).\end{aligned} \tag{15}$$

Here, $\boldsymbol{h}_k$ corresponds to an augmented virtual array $\mathbb{S} = \{0, d_r, \cdots, (N_tN_r-1)d_r\}$, where

$$\boldsymbol{A}_{\mathbb{S}}(\boldsymbol{\theta}) = [\boldsymbol{a}_{\mathbb{S}}(\theta_1), \boldsymbol{a}_{\mathbb{S}}(\theta_2), \cdots, \boldsymbol{a}_{\mathbb{S}}(\theta_Q)] \tag{16}$$

is the steering matrix of the virtual array $\mathbb{S}$, and

$$\begin{aligned}\boldsymbol{a}_{\mathbb{S}}(\theta_q) &= \boldsymbol{a}_t(\theta_q) \otimes \boldsymbol{a}_r(\theta_q)\\ &= \left[1, e^{-j\frac{2\pi}{\lambda}d_r\sin\theta_q}, \cdots, e^{-j\frac{2\pi}{\lambda}(N_tN_r-1)d_r\sin\theta_q}\right]^{\mathrm{T}}\end{aligned} \tag{17}$$

is the steering vector corresponding to the q-th non-cooperative target.

Unlike the virtual array formed in (8), the augmented virtual array $\mathbb{S}$ corresponds to a single subcarrier, leading to the same propagation delay of all the virtual array antennas. Thus, the augmented virtual array $\mathbb{S}$ is a ULA. Moreover, since the vectorized virtual channels $\{\boldsymbol{h}_1, \boldsymbol{h}_2, \cdots, \boldsymbol{h}_K\}$ estimated on different subcarriers are independent, we can formulate a virtual channel matrix

$$\boldsymbol{H} = [\boldsymbol{h}_1, \boldsymbol{h}_2, \cdots, \boldsymbol{h}_K] = \boldsymbol{A}_{\mathbb{S}}\boldsymbol{B}\boldsymbol{E} + \Delta\tilde{\boldsymbol{G}}, \tag{18}$$

where

$$\boldsymbol{E} := [\boldsymbol{e}_1, \boldsymbol{e}_2, \cdots, \boldsymbol{e}_K] \tag{19}$$

is the matrix of propagation delay, and $\Delta\tilde{\boldsymbol{G}} = [\mathrm{vec}(\Delta\boldsymbol{G}_1), \mathrm{vec}(\Delta\boldsymbol{G}_2), \cdots, \mathrm{vec}(\Delta\boldsymbol{G}_K)]$ is the sensing channel estimation error matrix. The formulation of $\boldsymbol{H}$ can be regarded as sampling the equivalent Q signals utilizing K uncorrelated observations simultaneously with the virtual array $\mathbb{S}$. The covariance of virtual channel matrix is then calculated as

$$\boldsymbol{\Gamma} = \frac{1}{K}\boldsymbol{H}\boldsymbol{H}^{\mathrm{H}} = \frac{1}{K}\boldsymbol{A}_{\mathbb{S}}\underbrace{\boldsymbol{B}\boldsymbol{E}\boldsymbol{E}^{\mathrm{H}}\boldsymbol{B}^{\mathrm{H}}}_{\boldsymbol{\Xi}}\boldsymbol{A}_{\mathbb{S}}^{\mathrm{H}} + \frac{1}{K}\Delta\tilde{\boldsymbol{G}}\Delta\tilde{\boldsymbol{G}}^{\mathrm{H}}. \tag{20}$$

Here, we define $\boldsymbol{\Xi} := \boldsymbol{B}\boldsymbol{E}\boldsymbol{E}^{\mathrm{H}}\boldsymbol{B}^{\mathrm{H}}$ as an equivalent signal matrix, and $\boldsymbol{\Xi}$ is full-rank when the distances of targets are different, i.e., $R_i \neq R_j$ if $i \neq j$, for $i, j \in \{1, 2, \cdots, Q\}$. This enables the subsequent computation of DOAs. However, when the targets have the same distance, $\boldsymbol{\Xi}$ becomes rank-deficient, and the corresponding solution will be elaborated in the next section.

In order to retrieve angle information from $\boldsymbol{\Gamma}$ in (20), the subspace processing is incorporated, where a spectrum can be constructed utilizing the orthogonality between the

signal subspace and noise subspace, and angles can be then estimated by peak searching of the spectrum. Thus, we perform eigen-decomposition on $\boldsymbol{\Gamma}$ as $\boldsymbol{\Gamma} = \boldsymbol{U}\boldsymbol{\Sigma}\boldsymbol{U}^{\mathrm{H}}$, where the diagonal matrix $\boldsymbol{\Sigma}$ contains N_tN_r eigenvalues, and $\boldsymbol{U}$ is the matrix with corresponding orthogonal eigenvectors as its columns. Since there are Q non-zero eigenvalues in $\boldsymbol{\Sigma}$, the matrix $\boldsymbol{U}$ can be expressed as $\boldsymbol{U} = [\boldsymbol{U}_1\ \boldsymbol{U}_2]$, where $\boldsymbol{U}_1 \in \mathbb{C}^{N_tN_r \times Q}$ contains Q eigenvectors corresponding to Q largest eigenvalues, and $\boldsymbol{U}_2 \in \mathbb{C}^{N_tN_r \times (N_tN_r - Q)}$ contains the eigenvectors corresponding to the rest eigenvalues. Since the basis vectors in $\boldsymbol{U}_2$ fall into the null space of the signal matrix, the estimation of DOAs $\hat{\theta}_q$ can be obtained by searching the peaks of the spectrum function $\frac{1}{\|\boldsymbol{a}_{\mathbb{S}}^{\mathrm{H}}(\theta)\boldsymbol{U}_2\|_{\mathrm{F}}^2}$ as

$$\hat{\theta}_q = \arg\max_{\theta} \frac{1}{\left\|\boldsymbol{a}_{\mathbb{S}}^{\mathrm{H}}(\theta)\boldsymbol{U}_2\right\|_{\mathrm{F}}^2},\ q = 1, 2, \cdots, Q, \tag{21}$$

where $\theta \in [-\pi, \pi]$ is the spectrum searching angle. Although the deployed system in this paper is consisted of linear arrays, the proposed algorithm can be extended for the estimation of azimuth and elevation angles of the non-cooperative targets when L-shaped array or planar array is utilized.

3.2 DOA estimation for targets at identical distance

When two targets has the numerically identical distance, the estimation of their DOAs using the proposed algorithm becomes a tricky problem. This is due to the fact that, the equivalent signal matrix $\boldsymbol{\Xi}$ in (20) is no longer full-rank under this circumstance. In particular, $\boldsymbol{\Xi}$ obeys the following property.

Theorem 1 *For any* $i,\ j \in \{1, 2, \cdots, Q\}$ $(Q < K)$ *and* $i \neq j$, *if* $R_i = R_j$, *then* $\boldsymbol{\Xi}$ *is rank-deficient.*

1 ***Proof***

As the transmission attenuation matrix $\boldsymbol{B}$ *contains non-zero elements on the diagonal, it is full-rank, i.e.,* $\mathrm{rank}(\boldsymbol{B}) = Q$. *Thus, we have* $\mathrm{rank}(\boldsymbol{B}\boldsymbol{E}\boldsymbol{E}^{\mathrm{H}}\boldsymbol{B}^{\mathrm{H}}) \leq \min\left\{\mathrm{rank}(\boldsymbol{B}^{\mathrm{H}}), \mathrm{rank}(\boldsymbol{B}\boldsymbol{E}\boldsymbol{E}^{\mathrm{H}})\right\} = \mathrm{rank}(\boldsymbol{B}\boldsymbol{E}\boldsymbol{E}^{\mathrm{H}})$ *and we also have* $\mathrm{rank}(\boldsymbol{B}\boldsymbol{E}\boldsymbol{E}^{\mathrm{H}}) \leq \min\{\mathrm{rank}(\boldsymbol{B}), \mathrm{rank}(\boldsymbol{E}\boldsymbol{E}^{\mathrm{H}})\} = \mathrm{rank}(\boldsymbol{E}\boldsymbol{E}^{\mathrm{H}})$, *which lead to* $\mathrm{rank}(\boldsymbol{B}\boldsymbol{E}\boldsymbol{E}^{\mathrm{H}}\boldsymbol{B}^{\mathrm{H}}) \leq \mathrm{rank}(\boldsymbol{E}\boldsymbol{E}^{\mathrm{H}})$. *Likewise, it holds that* $\mathrm{rank}(\boldsymbol{E}\boldsymbol{E}^{\mathrm{H}}) \leq \min\{\mathrm{rank}(\boldsymbol{B}^{-1}), \mathrm{rank}(\boldsymbol{B}\boldsymbol{E}\boldsymbol{E}^{\mathrm{H}})\} = \mathrm{rank}(\boldsymbol{B}\boldsymbol{E}\boldsymbol{E}^{\mathrm{H}}) \leq \min\{\mathrm{rank}(\boldsymbol{B}\boldsymbol{E}\boldsymbol{E}^{\mathrm{H}}\boldsymbol{B}^{\mathrm{H}}), \mathrm{rank}(\boldsymbol{B}^{-\mathrm{H}})\}$, *leading to* $\mathrm{rank}(\boldsymbol{E}\boldsymbol{E}^{\mathrm{H}}) \leq \mathrm{rank}(\boldsymbol{B}\boldsymbol{E}\boldsymbol{E}^{\mathrm{H}}\boldsymbol{B}^{\mathrm{H}})$. *Therefore, we have* $\mathrm{rank}(\boldsymbol{E}\boldsymbol{E}^{\mathrm{H}}) = \mathrm{rank}(\boldsymbol{B}\boldsymbol{E}\boldsymbol{E}^{\mathrm{H}}\boldsymbol{B}^{\mathrm{H}})$. *We then focus on the rank of* $\boldsymbol{E}\boldsymbol{E}^{\mathrm{H}}$. *According to (4) and (19),* $\boldsymbol{E}\boldsymbol{E}^{\mathrm{H}}$ *is represented as*

$$\boldsymbol{E}\boldsymbol{E}^{\mathrm{H}} = \begin{bmatrix} K & \sum_{k=1}^{K} e^{-j2\pi k\Delta f \frac{2(R_1-R_2)}{c}} & \cdots & \sum_{k=1}^{K} e^{-j2\pi k\Delta f \frac{2(R_1-R_Q)}{c}} \\ \sum_{k=1}^{K} e^{-j2\pi k\Delta f \frac{2(R_2-R_1)}{c}} & K & \cdots & \sum_{k=1}^{K} e^{-j2\pi k\Delta f \frac{2(R_2-R_Q)}{c}} \\ \vdots & \vdots & \ddots & \vdots \\ \sum_{k=1}^{K} e^{-j2\pi k\Delta f \frac{2(R_Q-R_1)}{c}} & \sum_{k=1}^{K} e^{-j2\pi k\Delta f \frac{2(R_Q-R_2)}{c}} & \cdots & K \end{bmatrix}. \tag{22}$$

We can see that for $i \neq j$, if $R_i = R_j$, the i-th and the j-th columns of $\boldsymbol{E}\boldsymbol{E}^{\mathrm{H}}$ will be identical, such that the rank of $\boldsymbol{E}\boldsymbol{E}^{\mathrm{H}}$ will collapse into $Q-1$. Thus, $\boldsymbol{\Xi}$ is rank-deficient.

The rank deficiency of $\boldsymbol{\Xi}$ invalids the eigen-decomposition-based DOA estimation in (21). Hence, we propose the Toeplitz reconstruction to compensate the rank of the equivalent signal matrix $\boldsymbol{\Xi}$. To be specific, let $\boldsymbol{\Lambda}$ be the following block-wise Toeplitz matrix,

$$\boldsymbol{\Lambda} = \begin{bmatrix} \boldsymbol{H}(L,:) & \boldsymbol{H}(L-1,:) & \cdots & \boldsymbol{H}(1,:) \\ \boldsymbol{H}(L+1,:) & \boldsymbol{H}(L,:) & \cdots & \boldsymbol{H}(2,:) \\ \vdots & \vdots & \ddots & \vdots \\ \boldsymbol{H}(2L-1,:) & \boldsymbol{H}(2L-2,:) & \cdots & \boldsymbol{H}(L,:) \end{bmatrix}, \tag{23}$$

where L equals to $\lfloor \frac{N_t N_r+1}{2} \rfloor$. Then, the auto-correlation of $\boldsymbol{\Lambda}$ can be formulated as

$$\begin{aligned} \tilde{\boldsymbol{\Gamma}} &= \frac{1}{L}\boldsymbol{\Lambda}\boldsymbol{\Lambda}^{\mathrm{H}} \\ &= \frac{1}{L}\begin{bmatrix} \boldsymbol{H}(1:L,:) \\ \boldsymbol{H}(2:L+1,:) \\ \vdots \\ \boldsymbol{H}(L:2L-1,:) \end{bmatrix}\begin{bmatrix} \boldsymbol{H}(1:L,:) \\ \boldsymbol{H}(2:L+1,:) \\ \vdots \\ \boldsymbol{H}(L:2L-1,:) \end{bmatrix}^{\mathrm{H}} \\ &= \frac{1}{L}\sum_{l=1}^{L} \boldsymbol{J}_l \boldsymbol{H}\boldsymbol{H}^{\mathrm{H}} \boldsymbol{J}_l^{\mathrm{H}}, \end{aligned} \tag{24}$$

where

$$\mathbf{J}_l = \begin{bmatrix} \mathbf{0}_{L\times(l-1)} & \boldsymbol{I}_{L\times L} & \mathbf{0}_{L\times(L-l)} \end{bmatrix} \tag{25}$$

is a selection matrix, $l = 1, 2, \cdots, L$. Here, l denotes the index of the selected part of the augmented virtual array, and it is numerically identical with the index of the first element of the selected array. By substituting (18) into (24), $\tilde{\boldsymbol{\Gamma}}$ can be reformulated as

$$\tilde{\boldsymbol{\Gamma}} = \frac{1}{L}\sum_{l=1}^{L} \underbrace{\boldsymbol{J}_l \boldsymbol{A}_{\mathbb{S}}}_{\boldsymbol{A}_l} \boldsymbol{\Xi} \underbrace{\boldsymbol{A}_{\mathbb{S}}^{\mathrm{H}} \boldsymbol{J}_l^{\mathrm{H}}}_{\boldsymbol{A}_l^{\mathrm{H}}} + \boldsymbol{\Psi}. \tag{26}$$

Here, $\boldsymbol{\Psi} = \frac{1}{L}\sum_{l=1}^{L} \boldsymbol{J}_l \Delta\tilde{\boldsymbol{G}} \Delta\tilde{\boldsymbol{G}}^{\mathrm{H}} \boldsymbol{J}_l^{\mathrm{H}}$ represents the transformed auto-correlation of $\Delta\tilde{\boldsymbol{G}}$, and $\boldsymbol{A}_l = [\boldsymbol{a}_l(\theta_1), \boldsymbol{a}_l(\theta_2), \cdots, \boldsymbol{a}_l(\theta_Q)]$ represents the steering matrix of the l-th selected array with L elements, where the steering vector is

$$\boldsymbol{a}_l = \left[e^{-j\frac{2\pi}{\lambda}(l-1)d_r \sin\theta_q}, e^{-j\frac{2\pi}{\lambda}l d_r \sin\theta_q}, \cdots, e^{-j\frac{2\pi}{\lambda}(l+L-2)d_r \sin\theta_q} \right]^{\mathrm{T}}, \tag{27}$$

as the selected part of $\boldsymbol{a}_{\mathbb{S}}$ in (17). Since the distance between a certain element of the l-th selected array and the corresponding element in the first selected array is decided by $(l-1)d_r$, the steering vector for a fixed direction θ_q for these two arrays is proportional by the scale factor $e^{-j\frac{2\pi}{\lambda}(l-1)d_r \sin\theta_q}$. Therefore, the steering matrix of the l-th selected array can be represented as

$$\boldsymbol{A}_l = \boldsymbol{A}_1 \underbrace{\mathrm{diag}(e^{-j\frac{2\pi}{\lambda}(l-1)d_r \sin\theta_1}, e^{-j\frac{2\pi}{\lambda}(l-1)d_r \sin\theta_2}, \cdots, e^{-j\frac{2\pi}{\lambda}(l-1)d_r \sin\theta_Q})}_{\boldsymbol{F}_l}, \tag{28}$$

where $\boldsymbol{F}_l$ denotes a phase shift diagonal matrix with Q scale factors. Then, by substituting (28) into (26), $\tilde{\boldsymbol{\Gamma}}$ is further expressed as

$$\tilde{\boldsymbol{\Gamma}} = \frac{1}{L}\sum_{l=1}^{L} \boldsymbol{A}_l \boldsymbol{\Xi} \boldsymbol{A}_l^{\mathrm{H}} + \boldsymbol{\Psi} = \frac{1}{L}\boldsymbol{A}_1 \sum_{l=1}^{L} \left(\boldsymbol{F}_l \boldsymbol{\Xi} \boldsymbol{F}_l^{\mathrm{H}}\right) \boldsymbol{A}_1^{\mathrm{H}} + \boldsymbol{\Psi}. \tag{29}$$

A comparison between (20) and (29) reveals that, when $\boldsymbol{\Xi}$ is not full-rank, the rank of $\tilde{\boldsymbol{\Gamma}}$ is restored to Q by sacrificing the size of aperture. By substituting $\boldsymbol{\Gamma}$ with $\tilde{\boldsymbol{\Gamma}}$ for eigendecomposition, the true DOAs can be estimated even at presence of targets with identical distance.

3.3 Computational complexity analysis

In this section, we compare the computational complexities of the proposed algorithm to those of the MUSIC-based method [22], interleaving frame structure-based method [27] and the SSR-based method [31]. We assume that the distances of the targets are not identical, and thus the Toeplitz reconstruction is not considered for the proposed algorithm in this subsection.

The proposed algorithm involves sensing channel estimation and subspace-based DOA estimation, whose computational complexities are $\mathcal{O}\left(KN_t^2M + KN_t^2N_r + N_t^3 + N_tN_rM\right)$ and $\mathcal{O}\left(KN_t^2N_r^2 + N_t^3N_r^3 + N_t^2N_r^2P\right)$, where P denotes the number of spatial sampling grids. Since the interval of spatial sampling grids is set to 0.01° in this paper, the number of spatial sampling grids P equals to 18, 000, which is significantly larger than the other terms. Thus, the computational complexity of the proposed algorithm can be measured by $\mathcal{O}\left(N_t^2N_r^2P\right)$.

In comparison, the computational complexities of the interleaving frame structure-based method, the SSR-based method, and the MUSIC-based method are $\mathcal{O}(KN_rM + N_t^2N_r^2P + N_t^2N_r^2M + N_t^3N_r^3)$, $\mathcal{O}\left(N_tN_rMP^2\right)$ and $\mathcal{O}\left(KN_r^2M + N_r^3 + N_r^2P\right)$, respectively. Note that, method of exhaustion is employed to minimize the ℓ_1-norm, and the estimation results from all the symbols are averaged for the SSR-based method in this manuscript. Since the computational complexities of the interleaving frame structure-based method and the MUSIC-based method are dominated by the spectral peak searching procedures, they can be calculated as $\mathcal{O}\left(N_t^2N_r^2P\right)$ and $\mathcal{O}\left(N_r^2P\right)$, respectively. It is clear that the computational complexity of the SSR-based method is $MP/(N_tN_r)$ times higher than that of the proposed algorithm. Meanwhile, although the computational complexity of the MUSIC-based method can be smaller than that of the proposed algorithm, the DOA estimation performance of the MUSIC-based method is limited, since the virtual array derivation with larger aperture is not considered.

4 Simulation results and discussion

In this section, we evaluate the performance of the proposed nonorthogonal waveform assisted DOA estimation algorithm. The quadrature phase shift keying (QPSK) modulation is employed for OFDM symbols. The targets are characterized by (distance, direction, attenuation). The system parameters are listed in Table 1, in which the subcarrier spacing

and the carrier frequency obey the standard 38.101-1 of 3rd Generation Partnership Project (3GPP) for 5G wireless communication [39]. For simplicity, the CP symbol duration is neglected.

Assume that two far-field targets are respectively located at $(100m, \theta_1, 0.1)$ and $(50m, \theta_2, 0.1)$, where θ_1 and θ_2 are uniformly distributed in $[20°, 60°]$. The proposed algorithm is compared with MUSIC-based method with fully nonorthogonal transmitting principle [22], interleaving frame structure-based method with orthogonal transmitting principle [27] and the SSR-based method with partially orthogonal transmitting principle [31]. The interval of spatial sampling grids for all the methods is set to 0.01°. The root-mean-square error (RMSE) for DOA estimation

$$\mathrm{RMSE} = \sqrt{\frac{1}{LQ}\sum_{l=1}^{L}\sum_{q=1}^{Q}\left(\theta_{q,l} - \hat{\theta}_{q,l}\right)^2} \tag{30}$$

is adopted as the performance metric, where L represents the number of Monte-Carlo trials, $\theta_{q,l}$ denotes the DOA of the q-th target in the l-th trial, and $\hat{\theta}_{q,l}$ denotes its estimation. $L = 400$ Monte-Carlo trials are performed for each simulated scenario.

4.1 DOA estimation accuracy

First, since the number of deployed OFDM symbols and subcarriers are two important parameters that affect the DOA estimation accuracy, we present the DOA estimation accuracy with different number of employed OFDM symbols and subcarriers in Figs. 4 and 5, respectively. The signal-to-noise ratio (SNR), i.e., the ratio of average power of the received symbols to the noise power as $\mathrm{E}\left\{\boldsymbol{d}^{\mathrm{H}}\boldsymbol{d}\right\}/\mathrm{E}\left\{\boldsymbol{n}^{\mathrm{H}}\boldsymbol{n}\right\}$, is set to 0 dB. As shown in Fig. 4, the accuracy of proposed DOA estimation increases as the number of employed OFDM symbols increases. The reason is that the error of round-trip sensing channel estimation decreases with the increasing number of employed OFDM symbols, which benefits the accurate virtual channel matrix formation in (15) and (18). In contrast, the MUSIC-based method does not calculate the sensing channel nor synthesize a virtual array. Meanwhile, for the SSR-based method and the interleaving frame structure-based method, each OFDM symbol is separately considered, which means that the increasing number of OFDM symbols will not benefit the DOA estimation performance. The result in Fig. 5 suggests that the proposed algorithm enjoys an improved estimation accuracy

Table 1 System parameters

Parameter	Symbol	Value
Carrier frequency	f_c	28 GHz
Subcarrier spacing	Δf	60 kHz
Number of OFDM subcarriers	K	32
Number of employed OFDM symbols	M	100
Number of transmit antennas	N_t	4
Number of receive antennas	N_r	16
Transmit antenna spacing	d_t	8λ
Receive antenna spacing	d_r	0.5λ

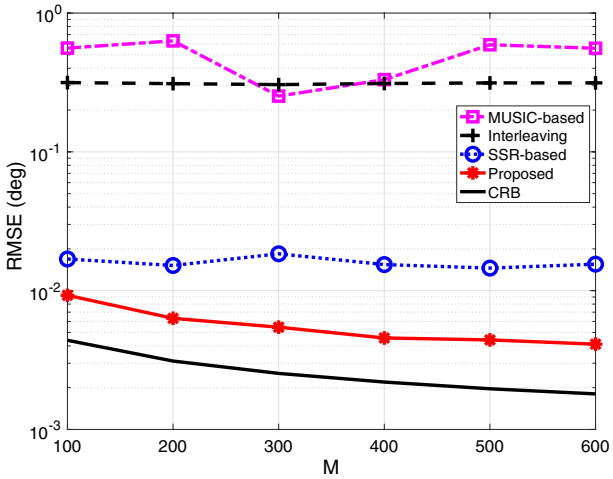

Fig. 4 DOA estimation accuracy comparison with different number of OFDM symbols

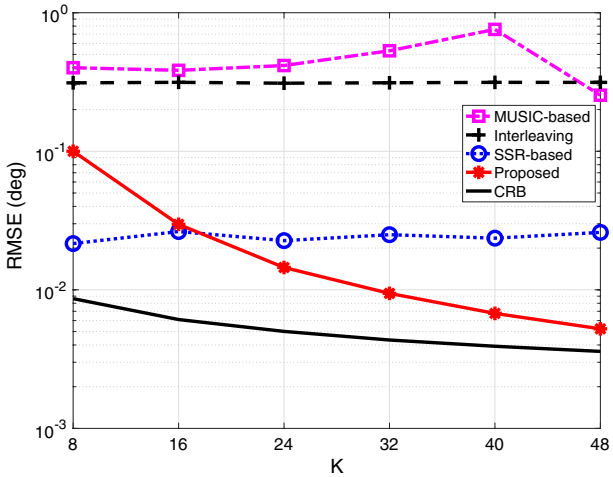

Fig. 5 DOA estimation accuracy comparison with different number of subcarriers

when more subcarriers are incorporated in the system. Note that, the SSR-based method has better DOA estimation accuracy than the proposed algorithm for $K < 16$ since the true distance values of the targets are utilized as a prior for the SSR-based method. However, the accuracy of the SSR-based performance is achieved at the cost of high computation complexity. More importantly, for both the interleaving frame structure-based method and the SSR-based method, the increasing number of subcarriers do not contribute to the improvement of estimation accuracy, because the subcarriers are independently considered for the virtual array formulation in (8).

Then, in Fig. 6, we compare the DOA estimation accuracy of the evaluated methods with differnet SNR. It is clear that the proposed algorithm outperforms the other methods. Benefiting from the construction of virtual channel matrix, the augmented virtual array can be derived under the fully nonorthogonal scenario. Thus, more pilot symbols can be effectively utilized for the proposed algorithm. Although the virtual arrays are also derived in the SSR-based method and the interleaving frame structure-based

method, they require orthogonal or partially orthogonal transmitting principles, thus the number of utilized pilot symbols is limited with respect to the fixed number of OFDM symbols and subcarriers.

4.2 Angular resolution

We also compare the angular resolution of all evaluated methods in Fig. 7. In particular, three targets are assumed, whose locations are $(50m, 44°, 0.1)$, $(100m, 46°, 0.2)$, and $(80m, 48°, 0.3)$, respectively. The SNR is set to 0 dB. Except the proposed algorithm, the other compared methods fail to distinguish all the targets. For the methods that consider the virtual array derivation in the orthogonal and partially orthogonal scenarios, the synthesized virtual arrays are not ULAs, as illustrated in Sect. 2. The estimation performance of the interleaving frame structure-based method is thereby affected. Although the SSR-based method does not rely on the ULA, its resolution is limited by predefined searching grid. In contrast, since each row of the virtual channel matrix in (18) corresponds to a single subcarrier, the virtual array derived in the proposed algorithm is a ULA, such that high DOA estimation resolution can be achieved.

In scenarios with targets at identical distance, it is necessary for the proposed algorithm to implement Toeplitz reconstruction, as shown in Fig. 8. Four far-field radar targets are assumed, which locate at $(50m, 44°, 0.1)$, $(100m, 46°, 0.2)$, $(80m, 48°, 0.3)$ and $(50m, 50°, 0.2)$, respectively. With Toeplitz reconstruction, the rank of the equivalent signal matrix $\boldsymbol{\Xi}$ in (20) is restored, such that the proposed algorithm can effectively estimate the DOAs of targets which locate at the identical distance.

4.3 Computational complexity

To demonstrate the computational complexities of the proposed algorithm and the compared methods intuitively, a comparison of computation time is depicted in Fig. 9. It is clear that the proposed algorithm has better computational efficiency than the SSR-based method and the interleaving frame structure-based method. The MUSIC-based method is computationally faster than the proposed algorithm since the dimension of the sample covariance matrix for the MUSIC-based method is lower than that for the

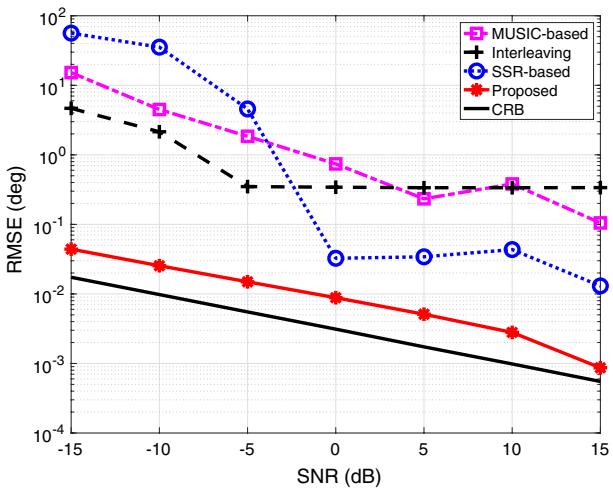

Fig. 6 DOA estimation accuracy comparison with differnet SNR of signals

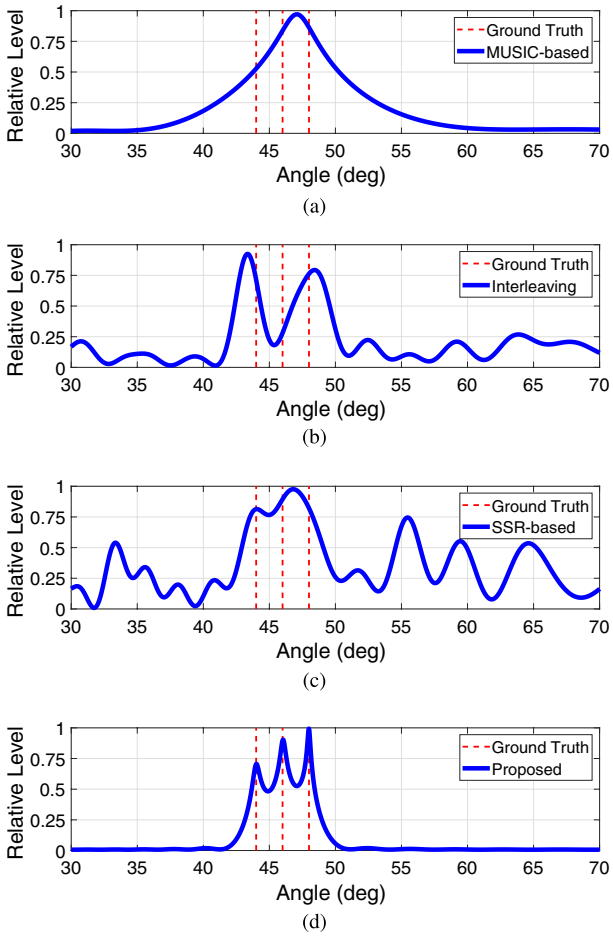

Fig. 7 Angular resolution comparison. **a** MUSIC-based method; **b** Interleaving frame structure-based method; **c** The SSR-based method; **d** The proposed algorithm

proposed algorithm. However, the MUSIC-based method suffers from a deteriorated DOA estimation performance, while the computation time of the proposed algorithm is still comparable.

5 Conclusion

In this paper, we have addressed the DOA estimation problem in a fully nonorthogonal joint MIMO sensing and communication scenario, while maintaining a high communication rate. To enhance the DOA estimation performance, an augmented virtual array with enlarged aperture is formulated by effectively using the coefficients of the round-trip sensing channels. Then, by treating the virtual channel matrix as the equivalent signal of the virtual array, the subspace processing is conducted for DOA estimation. To tackle the rank-deficiency problem of the equivalent signal matrix at the presence of targets with identical distance, the Toeplitz reconstruction is proposed to restore the rank. Simulation results demonstrate the superiority of the proposed algorithm over conventional methods in both estimation resolution and accuracy.

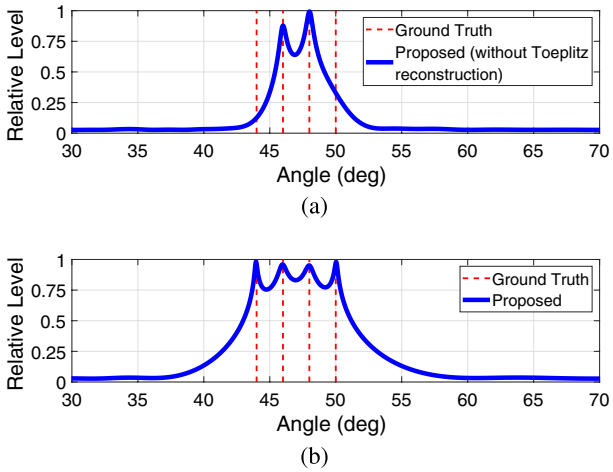

Fig. 8 Estimation performance of the proposed algorithm for targets at identical distance. **a** Proposed algorithm without Toeplitz reconstruction; **b** Proposed algorithm with Toeplitz reconstruction

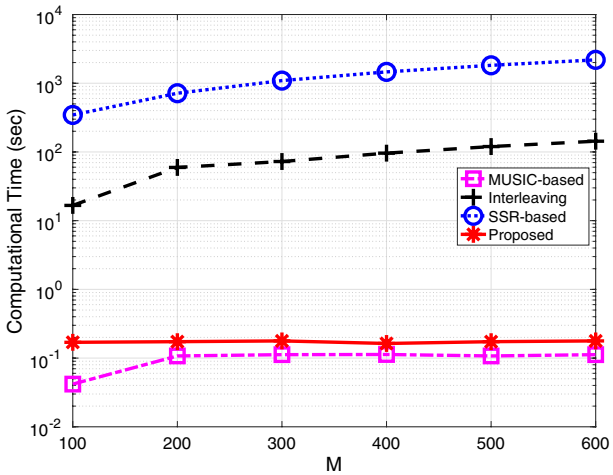

Fig. 9 DOA estimation accuracy comparison with differnet number of OFDM symbols

Abbreviations

A/D	Analog-to-digital
CP	Cyclic prefix
D/A	Digital-to-analog
DFT	Discrete Fourier transform
DOA	Direction-of-arrival
FR2	Frequency Range 2
GP	Guard period
LMMSE	Linear minimum mean square error
LS	Least square
MIMO	Multiple-input and multiple-output
MSE	Mean square error
MMSE	Minimum mean square error
OFDM	Orthogonal frequency-division multiplexing
P/S	Serial-to-parallel
PSK	Phase-shift keying
QAM	Quadrature amplitude modulation
QPSK	Quadrature phase shift keying
RMSE	Root-mean-square error
SNR	Signal-to-noise ratio
S/P	Parallel-to-serial

SSR	Sparse signal recovery
ULA	Uniform linear array
5G	Fifth-generation
5G NR	5G New Radio.

Acknowledgements
The authors would like to thank the editor and the anonymous reviewers for their helpful comments and suggestions.

Author contributions
All authors devoted equally to the manuscript. All authors read and approved the final manuscript.

Funding
This work was supported in part by the National Natural Science Foundation of China (No. U21A20456, 62271444, 61901413), Zhejiang Provincial Natural Science Foundation of China (No. LZ23F010007), Zhejiang University Education Foundation Qizhen Scholar Foundation, and the 5G Open Laboratory of Hangzhou Future Sci-Tech City.

Availability of data and materials
Data sharing is not applicable to this article as no datasets were generated or analyzed during the current study.

Declarations

Ethics approval and consent to participate
Not applicable.

Consent for publication
Not applicable.

Competing interests
The authors declare that they have no competing interests.

Received: 10 August 2022 Accepted: 16 January 2023
Published online: 08 February 2023

References

1. J.A. Zhang, M.L. Rahman, K. Wu, X. Huang, Y.J. Guo, S. Chen, J. Yuan, Enabling joint communication and radar sensing in mobile networks–A survey. IEEE Commun. Surv. Tut. **24**(1), 306–345 (2022)
2. L. Zheng, M. Lops, Y.C. Eldar, X. Wang, Radar and communication coexistence: An overview: A review of recent methods. IEEE Signal Process. Mag. **36**(5), 85–99 (2019)
3. A. Hassanien, M.G. Amin, Y.D. Zhang, F. Ahmad, Dual-function radar-communications: Information embedding using sidelobe control and waveform diversity. IEEE Trans. Signal Process. **64**(8), 2168–2181 (2016)
4. C. Shi, F. Wang, M. Sellathurai, J. Zhou, S. Salous, Power minimization-based robust OFDM radar waveform design for radar and communication systems in coexistence. IEEE Trans. Signal Process. **66**(5), 1316–1330 (2018)
5. F. Liu, Y. Cui, C. Masouros, J. Xu, T.X. Han, Y.C. Eldar, S. Buzzi, Integrated sensing and communications: Toward dual-functional wireless networks for 6G and beyond. IEEE J. Sel. Areas Commun. **40**(6), 1728–1767 (2022)
6. A. Hassanien, M.G. Amin, Y.D. Zhang, F. Ahmad, Signaling strategies for dual-function radar communications: An overview. IEEE Aerosp. Electron. Syst. Mag. **31**(10), 36–45 (2016)
7. M.L. Rahman, J.A. Zhang, X. Huang, Y.J. Guo, R.W. Heath, Framework for a perceptive mobile network using joint communication and radar sensing. IEEE Trans. Aerosp. Electron. Syst. **56**(3), 1926–1941 (2020)
8. A. Sakhnini, S. De Bast, M. Guenach, A. Bourdoux, H. Sahli, S. Pollin, Near-field coherent radar sensing using a massive MIMO communication testbed. IEEE Trans. Wireless Commun. **21**(8), 6256–6270 (2022)
9. Z. Mao, S. Liu, Y.D. Zhang, L. Han, Y. Huang, Joint DoA-range estimation using space-frequency virtual difference coarray. IEEE Trans. Signal Process. **70**, 2576–2592 (2022)
10. I.A. Hemadeh, K. Satyanarayana, M. El-Hajjar, L. Hanzo, Millimeter-wave communications: Physical channel models, design considerations, antenna constructions, and link-budget. IEEE Commun. Surv. Tut. **20**(2), 870–913 (2018)
11. M. Steinbauer, A.F. Molisch, E. Bonek, The double-directional radio channel. IEEE Antennas Propag. Mag. **43**(4), 51–63 (2001)
12. S. Zhang, A. Ahmed, Y.D. Zhang, S. Sun, Enhanced DOA estimation exploiting multi-frequency sparse array. IEEE Trans. Signal Process. **69**, 5935–5946 (2021)
13. C. Zhou, Y. Gu, X. Fan, Z. Shi, G. Mao, Y.D. Zhang, Direction-of-arrival estimation for coprime array via virtual array interpolation. IEEE Trans. Signal Process. **66**(22), 5956–5971 (2018)
14. Z. Ni, J.A. Zhang, X. Huang, K. Yang, F. Gao, Parameter estimation and signal optimization for joint communication and radar sensing. In Proc. IEEE Int. Conf. Commun. Workshops (ICC), (Dublin, Ireland, 2020), pp. 1–6
15. C. Zhou, Y. Gu, Z. Shi, Y.D. Zhang, Off-grid direction-of-arrival estimation using coprime array interpolation. IEEE Signal Process. Lett. **25**(11), 1710–1714 (2018)
16. M.F. Keskin, H. Wymeersch, V. Koivunen, MIMO-OFDM joint radar-communications: Is ICI friend or foe? IEEE J. Sel. Topics Signal Process. **15**(6), 1393–1408 (2021)
17. Y. Gu, A. Leshem, Robust adaptive beamforming based on interference covariance matrix reconstruction and steering vector estimation. IEEE Trans. Signal Process. **60**(7), 3881–3885 (2012)

18. H. Zheng, C. Zhou, Z. Shi, Y. Gu, Structured tensor reconstruction for coherent DOA estimation. IEEE Signal Process. Lett. **29**, 1634–1638 (2022)
19. G.L. Stuber, J.R. Barry, S.W. McLaughlin, Y. Li, M.A. Ingram, T.G. Pratt, Broadband MIMO-OFDM wireless communications. Proc. IEEE **92**(2), 271–294 (2004)
20. S.D. Liyanaarachchi, C. Baquero Barneto, T. Riihonen, M. Heino, M. Valkama, Range–angle processing for target detection in joint MIMO-OFDM communications and sensing. In Proc. IEEE Workshop Signal Process. Adv. Wireless Commun. (SPAWC), (Lucca, Italy, 2021), pp. 486–490
21. L. Pucci, E. Matricardi, E. Paolini, W. Xu, A. Giorgetti, Performance analysis of joint sensing and communication based on 5G New Radio. In Proc. IEEE Glob. Commun. Conf. (GLOBECOM), (Madrid, Spain, 2021), pp. 1–6
22. L. Pucci, E. Paolini, A. Giorgetti, System-level analysis of joint sensing and communication based on 5G New Radio. IEEE J. Sel. Areas Commun. **40**(7), 2043–2055 (2022)
23. Z. Ni, J.A. Zhang, X. Huang, K. Yang, J. Yuan, Uplink sensing in perceptive mobile networks with asynchronous transceivers. IEEE Trans. Signal Process. **69**, 1287–1300 (2021)
24. L. Pucci, E. Matricardi, E. Paolini, W. Xu, A. Giorgetti, Performance analysis of a bistatic joint sensing and communication system. In Proc. IEEE Int. Conf. Commun. Workshops (ICC), (Seoul, Korea, 2022), pp. 73–78
25. J. Li, P. Stoica, MIMO radar with colocated antennas. IEEE Signal Process. Mag. **24**(5), 106–114 (2007)
26. C. Sturm, T. Zwick, W. Wiesbeck, An OFDM system concept for joint radar and communications operations. In Proc. IEEE Veh. Technol. Conf. (VTC), (Barcelona, Spain, 2009), pp. 1–5
27. C. Sturm, W. Wiesbeck, Waveform design and signal processing aspects for fusion of wireless communications and radar sensing. Proc. IEEE **99**(7), 1236–1259 (2011)
28. Y. Liu, G. Liao, Z. Yang, J. Xu, Joint range and angle estimation for an integrated system combining MIMO radar with OFDM communication. Multidimens. Syst. Signal Process. **30**(2), 661–687 (2019)
29. X. Wang, A. Hassanien, M.G. Amin, Sparse transmit array design for dual-function radar communications by antenna selection. Digit. Signal Process. **83**, 223–234 (2018)
30. Z. Cheng, B. Liao, QoS-aware hybrid beamforming and DOA estimation in multi-carrier dual-function radar-communication systems. IEEE J. Sel. Areas Commun. **40**(6), 1890–1905 (2022)
31. Z. Xu, A. Petropulu, A wideband dual function radar communication system with sparse array and OFDM waveforms. arXiv: 2106.05878 (2021)
32. B. Liao, Fast angle estimation for MIMO radar with nonorthogonal waveforms. IEEE Trans. Aerosp. Electron. Syst. **54**(4), 2091–2096 (2018)
33. G. Zheng, DOA estimation in MIMO radar with non-perfectly orthogonal waveforms. IEEE Commun. Lett. **21**(2), 414–417 (2017)
34. H. Zheng, Z. Shi, C. Zhou, M. Haardt, J. Chen, Coupled coarray tensor CPD for DOA estimation with coprime L-shaped array. IEEE Signal Process. Lett. **28**, 1545–1549 (2021)
35. Z. Shi, C. Zhou, Y. Gu, N.A. Goodman, F. Qu, Source estimation using coprime array: A sparse reconstruction perspective. IEEE Sensors J. **17**(3), 755–765 (2017)
36. C. Zhou, Y. Gu, S. He, Z. Shi, A robust and efficient algorithm for coprime array adaptive beamforming. IEEE Trans. Veh. Technol. **67**(2), 1099–1112 (2018)
37. V. Savaux, Y. Louët, LMMSE channel estimation in OFDM context: A review. IET Signal Process. **11**(2), 123–134 (2017)
38. Y. Liu, Z. Tan, H. Hu, L.J. Cimini, G.Y. Li, Channel estimation for OFDM. IEEE Commun. Surv. Tut. **16**(4), 1891–1908 (2014)
39. 3GPP: NR; User Equipment (UE) radio transmission and reception; Part 1: Range 1 Standalone. Technical Specification (TS) 38.101-1, 3rd Generation Partnership Project (3GPP) (2021). Version 17.3.0. http://www.3gpp.org/-DynaReport/-38101-1.htm

Publisher's Note